Energies **2015**, *8*, 1547-1560; doi:10.3390/en8031547

OPEN ACCESS

energies

ISSN 1996-1073

www.mdpi.com/journal/energies

Article

Effect of Extended Extinction from Gold Nanopillar Arrays on the Absorbance Spectrum of a Bulk Heterojunction Organic Solar Cell

Shu-Ju Tsai [1,2,†], Mihaela Ballarotto [2,3], Hung-Chih Kan [1,2,4] and Raymond J. Phaneuf [1,2,3,*]

[1] Department of Materials Science and Engineering, University of Maryland, College Park, MD 20740, USA; E-Mails: phoebe@mail.ncku.edu.com (S.-J.T.); hungchih.kan@outlook.com (H.-C.K.)

[2] Laboratory for Physical Sciences, College Park, MD 20740, USA; E-Mail: mihaela@lps.umd.edu

[3] Department of Electrical and Computer Engineering, University of Maryland, College Park, MD 20742, USA

[4] Department of Physics, National Chung-Cheng University, Tainan 701, Taiwan

[†] Current address: Center for Micro/Nano Science and Technology, National Cheng Kung University, Tainan 701, Taiwan.

[*] Author to whom correspondence should be addressed; E-Mail: phaneuf@umd.edu; Tel.: +1-301-405-6566; Fax: +1-301-314-2029.

Academic Editor: I. M. Dharmadasa

Received: 7 November 2014 / Accepted: 14 January 2015 / Published: 18 February 2015

Abstract: We report on the effects of enhanced absorption/scattering from arrays of Au nanopillars of varied size and spacing on the spectral response of a P3HT:PCBM bulk heterojunction solar cell. Nanopillar array-patterned devices do show increased optical extinction within a narrow range of wavelengths compared to control samples without such arrays. The measured external quantum efficiency and calculated absorbance, however, both show a decrease near the corresponding wavelengths. Numerical simulations indicate that for relatively narrow nanopillars, the increased optical extinction is dominated by absorption within the nanopillars, rather than scattering, and is likely dissipated by Joule heating.

Keywords: organic solar cells; plasmonics; nanostructures

1. Introduction

There is presently a great deal of interest in the possibility of using the strong coupling between light and particle plasmons in noble metal nanostructures as a means of increasing the efficiency of organic solar cells (OSCs). Existing bulk-heterojunction (BHJ) OSCs produce power conversion efficiencies of less than 10% [1,2], *i.e.*, less than half of what can be realized in single crystal silicon-based devices [3]. This is in part because of the relatively narrow optical wavelength range in which typical donor and acceptor molecules absorb strongly. Seemingly the tunability of particle plasmon resonances via variation of their shapes, size, and dielectric environment should allow a broader spectral absorption range [4] for hybrid metallic nanostructure/OSC devices, which might be expected to produce enhanced solar cell efficiency [5–10], as has been found for Si-based devices [11]. Reports of the efficacy of this approach [5–10,12] however are contradictory. Some, based upon simple transmission measurements and/or external quantum efficiency (EQE) measurements [5–9] of BHJ OSC devices which incorporated small (*i.e.*, <50 nm in diameter) Ag or Au nanospheres, indicate an increase in the efficiency. For example, Mofa, *et al.* [5] reported an increased power conversion efficiency, from 1.3% to 2.2%, on incorporation of silver nanospheres in a BHJ solar cell; however the device with Ag nanospheres exhibited a decrease in external quantum efficiency at the peak wavelength in extinction spectrum (450 nm). In contrast, a recent report by Topp, *et al.* [12] indicated that incorporation of small Au nanospheres into the poly(3-hexylthiophene) (P3HT) and [6,6]-phenyl C61 butyric acid methyl ester (PCBM) active layer of a BHJ organic device results in a significant decrease in power conversion efficiency [12]. A limitation of conventional transmission measurements is that they detect light intensity in the far field, but do not allow direct discrimination as to whether the light is absorbed or scattered within the active layer of a functional OSC device containing nanostructures. Recently [13] we have shown that there is good correspondence between the measured external quantum efficiency of an OSC containing a Au nanopillar array and the calculated optical absorption within the active layer. In this paper we extend those results to determine the optical absorption within the Au nanopillars, and address the issue of the cause for the decrease in the solar cell efficiency that we observed, and how it depends on the pillar size and spacing.

2. Results and Discussion

Our device architecture is shown in Figure 1, and described in detail in the Experimental Section. Briefly, Au nanopillars of varied size and spacing are patterned onto a transparent indium tin oxide electrode onto which a PCBM/P3HT mixture is deposited, followed by capping with a nonstoichiometric titanium oxide (TiO_x) layer. As will be seen below, the absence of a hole conduction layer such as PEDOT:PSS above the transparent electrode results in a relatively low overall external quantum efficiency. However the central point of this work is to investigate the effect of plasmonic resonance of noble metal particles on the efficiency of the OSCs, not to achieve an optimized design which includes such an effect. Our focus in this work is to explore the relationship between the optical extinction spectrum and external quantum efficiency of our OSC devices; we reported on the performance of similar devices under simulated solar illumination elsewhere [13]. In this work we first carried out transmission spectrum measurements. We calculate the extinction from the measured transmission using:

$$Extinction = 1 - \frac{T_{Sample}}{T_{Sub}} \quad (1)$$

where T_{Sample} is the transmission for a given sample and T_{Sub} is that for an ITO-coated glass substrate. As we discuss below, we observed peaks in the extinction spectra, typically identified with excitation of localized surface plasmons [14–16].

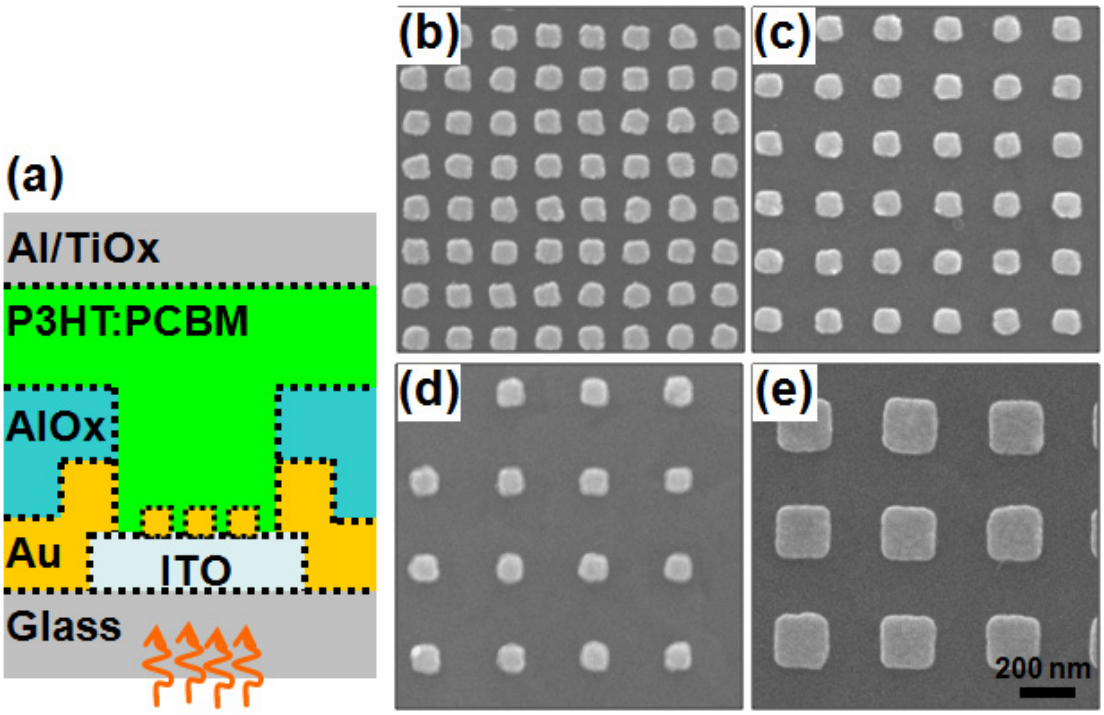

Figure 1. (**a**) Schematic cross section of the NP-patterned organic solar cell design studied in this work; (**b**–**e**) SEM images of Au nanopillar arrays on ITO surface with pillars (**b**) 95 nm wide × 150 nm pitch; (**c**) 95 nm wide × 200 nm pitch; (**d**) 95 nm wide × 300 nm pitch; and (**e**) 180 nm wide × 360 nm pitch, respectively. The pillar heights are 70 nm in each case.

Figure 2a shows the results of transmission measurements through nanopillar arrays on ITO-coated glass substrates. For the NP array with width W = 95 nm and pitch P = 150 nm, the measured peak in the extinction occurs at 596 ± 3 nm optical wavelength (purple curve). On increasing the pitch the peak in extinction slightly shifts toward longer wavelengths, 604 ± 2 nm at a pitch of 200 nm (red curve), and 609 ± 2 nm at a pitch of 300 nm (green curve). The slight red shift in the peak in extinction with increasing pitch, can be attributed to the effect of radiative dipole coupling [14]. For the array with W = 180 nm × P = 360 nm, the most intense peak in extinction occurs at a wavelength of 680 ± 4 nm (blue curve). This red shift in the peak in extinction as the NP width increases is consistent with the known behavior of localized surface plasmon resonances [14,17,18].

Figure 2b shows the experimentally derived extinction spectra for a P3HT:PCBM film deposited on a non-NP-patterned substrate (black curve), for a P3HT:PCBM film on an Au NP array with W = 95 nm × P = 200 nm (red curve), and for a P3HT:PCBM film-coated NP array with W = 180 nm × P = 360 nm (blue curve). The thickness of the P3HT:PCBM film, as determined by profilometer measurements, was approximately 168 nm. Its presence produces a red shift in the extinction peaks, consistent with the increase in dielectric constant of the medium surrounding the

nanopillars [14]. The measured red shifts are from approximately 604 nm to 657 nm for NP arrays with W = 95 nm × P = 200 nm, and from 680 nm to 830 nm for NP arrays with W = 180 nm × P = 360 nm. Figure 2b also shows a second, less intense NP-associated peak in the extinction spectrum for the W = 180 nm × P = 360 nm arrays near λ = 660 nm, apparently due to a higher-order particle plasmon mode; it is red shifted from λ ~ 560 nm for the bare NP array, and less intense than the peak for the W = 95 nm arrays. The peak in extinction for P3HT:PCBM-coated NP arrays with W = 95 nm × P = 150 nm occurs at approximately 650 nm (curve not shown). We did not measure the extinction spectrum for P3HT:PCBM-coated nanopillar arrays with W = 95 nm × P = 300 nm, but extrapolating the red shift based upon that for samples with pitch 150 nm and 200 nm, would give a peak at approximately 664 nm.

The results presented above are consistent with an increase in the optical extinction due to excitation of particle plasmons in our NP array-containing OSC devices. We next examine whether this results in an associated broadening in the absorption spectrum of the P3HT:PCBM layer, and in the EQE spectrum of OSC devices.

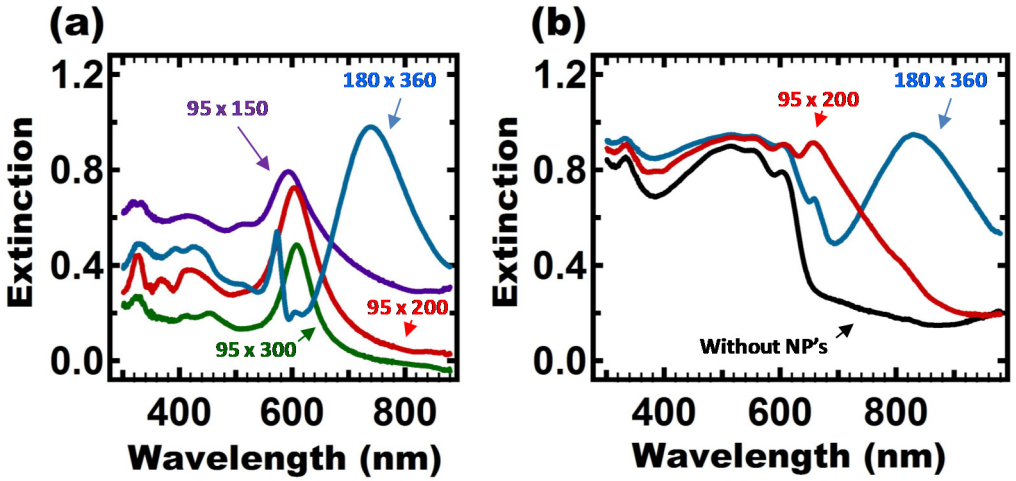

Figure 2. (**a**) Extinction spectra from NP-patterned arrays on ITO-coated glass substrates with 95 nm wide × 150 nm pitch pillars (purple curve), with 95 nm wide × 200 nm pitch pillars (red curve), with 95 nm wide × 300 nm pitch pillars (green curve), and with 180 nm wide × 360 nm pitch pillars (blue curve); (**b**) Corresponding extinction spectra after coating with a 168 nm thick layer of P3HT:PCBM. The red curve is for NP arrays with W = 95 nm wide × P = 200 nm, the blue curve is for that with W = 180 nm × P = 360 nm, and the black curve is for P3HT:PCBM on ITO- coated glass substrate.

Measured external quantum efficiency (EQE) spectra for devices with (red curves) and without (black curves) arrays of NPs are shown in in Figure 3a,d. The differences in the overall level of the EQE spectra for cells without NP's we attribute to variation in the phase separated domain structure within the active layer, which is sensitive to the details of the deposition and annealing; an advantage of our sample design is that it allows a direct comparison of the EQE between cells with and without NP's on the same substrate so that the effects of such differences are minimized. The pillar widths and pitches for these spectra are (a) W = 95 nm × P = 150 nm, (b) W = 95 nm × P = 200 nm; (c) W = 95 nm × P = 300 nm, and (d) W = 180 nm × P = 360 nm. Comparison of the NP array and control spectra in Figure 3a–c shows that for the W = 95 nm arrays there is no enhancement in the

EQE at the wavelengths where we observe peaks in the extinction spectra (*i.e.*, 650 nm, 657 nm, and 664 nm, respectively). The NP-associated peaks in extinction for the smaller, 95 nm width nanopillars do not give rise to enhanced solar cell efficiency. Instead they show a decrease in EQE near the optical wavelengths corresponding to NP-associated peaks in the extinction. In contrast, for the wider, W = 180 nm pillars (red curve in Figure 3d) a slight increase in the EQE is observed in the wavelength range from approximately 640 nm ~ 720 nm, bracketing the less intense peak in the extinction spectrum.

To understand the lack of simple correspondence between NP-associated peaks in the optical extinction and the measured EQE spectra for the W = 95 nm NP arrays, we calculate the absorbance within the P3HT:PCBM layer. Our previous results demonstrated that the calculated organic layer-absorbance is in good semi-quantitative agreement with the measured EQE of a NP array-patterned OSC [13]. The details of the calculation were discussed previously [13]. Based upon the observed corner rounding in our SEM images we approximated the W = 95 nm pillars as cylindrical, but used square cross sections for larger W = 180 nm pillars. Figure 3e–h show calculated absorbance spectra, corresponding to the measured EQE spectra for the devices of Figure 3a–d. The agreement is good between the calculated absorbance and measured EQE, both for the devices with (green curves in Figure 3e–g) and without (black curve; reproduced in each of Figure 3e–g for ease of direct comparison). We note that there is considerable rounding of the corners of the 95 nm wide Au pillars. We investigated the effect that this might have by comparing the calculated absorption for the square cross section pillars with the extreme case of cylindrical pillars. As shown in the supplementary material (Figure S1) this produces only very minor changes in the calculated spectrum, so that the agreement with the measured EQE remains good. The overall EQE for the device without nanopillar arrays is larger, in particular at wavelengths less than approximately 620 nm. We find that the reduction in both EQE and in calculated absorbance in this region increases monotonically with the area fraction covered by Au nanopillars, indicating that it is mainly due to the limited light transmitted through the arrays into the active layer. Consistent with the measured EQE spectra, the calculated P3HT:PCBM absorbance spectra for the NP-patterned devices with W = 95 nm (Figure 3e–g) are lower than that for the control device in the spectral region corresponding to the peaks in extinction. For the NP-patterned device with W = 180 nm, the absorbance is enhanced in the region from approximately from 620 nm to 700 nm, again qualitatively consistent with what we observe in the measured EQE spectra. Our earlier calculations indicated that this enhancement is associated with interference and diffraction effects due to presence of Au nanopillar arrays [13]. To make a more detailed comparison, we calculated the ratios of both the EQE and absorption spectra, with and without NP arrays as a function of pillar width and pitch. The ratio curves for the absorbance (green curves) and EQE (red curves), shown in Figure 3i–k, are similar in shape; both show dips near 650 nm, with a slight blue shift in that of the EQE relative to that in the absorbance, and with an overall red shift as the pitch of the array is increased. These dips are seemingly associated with the measured peaks in optical extinction, *i.e.*, that peaks in extinction correspond to dips in the EQE, at least for the smaller 95 nm width NP's we investigated. This result is qualitatively consistent with Morfa's [5] findings but conflicts with Lee's [6] report of an increase in measured EQE at the peak wavelength in the extinction spectrum for a device containing Au nanoparticles.

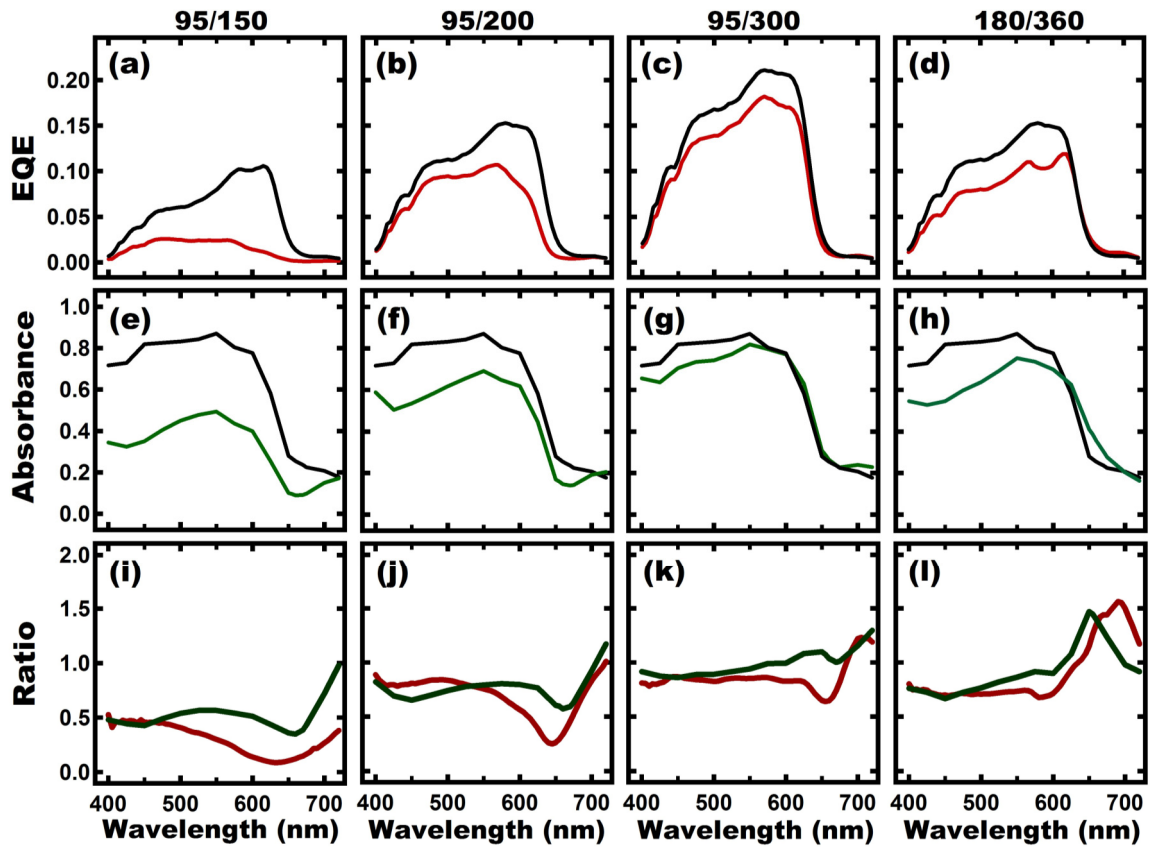

Figure 3. (**a**–**d**) Measured EQE for OSC devices with Au nanopillar arrays (red curves) and without (black curves); (**e**–**h**) Calculated P3HT:PCBM absorbance for devices with Au nanopillar arrays (green curves) and without (black curves); (**i**–**l**) Red curves are for ratios of measured EQE for devices with Au NP arrays and without and green curves are for ratios of calculated absorbance for devices with Au NP arrays and without. Panels from left to right are for Au NP-patterned cells with W = 95 nm × P = 150 nm, W = 95 nm × P = 200 nm, W = 95 nm × P = 300 nm, and W = 180 nm × P = 360 nm.

To reiterate, the motivation for the incorporation of noble metal nanoparticles in OSC devices is to enhance the optical absorbance in the organic active layer due to field enhancement associated with the particle plasmonic response to incident light. To return for a moment to the issue of the absence of the PEDOT:PSS layer in our devices, we note that some effect on the localized surface plasmon might be expected based on the change of the dielectric environment of the noble metal nanoparticles due the presence of this layer. However, since the typical thickness of the PEDOT:PSS layer (>70 nm) used for OSCs would place the active layer materials well beyond the range of the plasmonic evanescent field from the noble metal particles; we thus expect that the enhancement of the absorption would be even smaller if such a layer were present.

It is also interesting to note that for simpler geometries, the maximum field enhancement usually coincides with the peak in extinction [14], and thus with the expected enhancement in the EQE of an OSC device. This however is the opposite of what we have seen in the correspondence between our extinction measurements and the EQE measurement; it leads us to ask whether field enhancement within the organic layer does occur at wavelengths corresponding to particle plasmon excitation in our devices. Fluorescence maps of molecular films on metallic nanostructures have been demonstrated to

reveal the excitation of particle plasmon and surface plasmon resonances in such structures [17–21]; locations in the map where enhancement in fluorescence occurs indicate regions of localized field enhancement. The insert in Figure 4 shows a fluorescence map across three different P3HT:PCBM film-covered NP arrays on an ITO coated glass substrate (for this measurement no Al/TiOx layers were deposited).

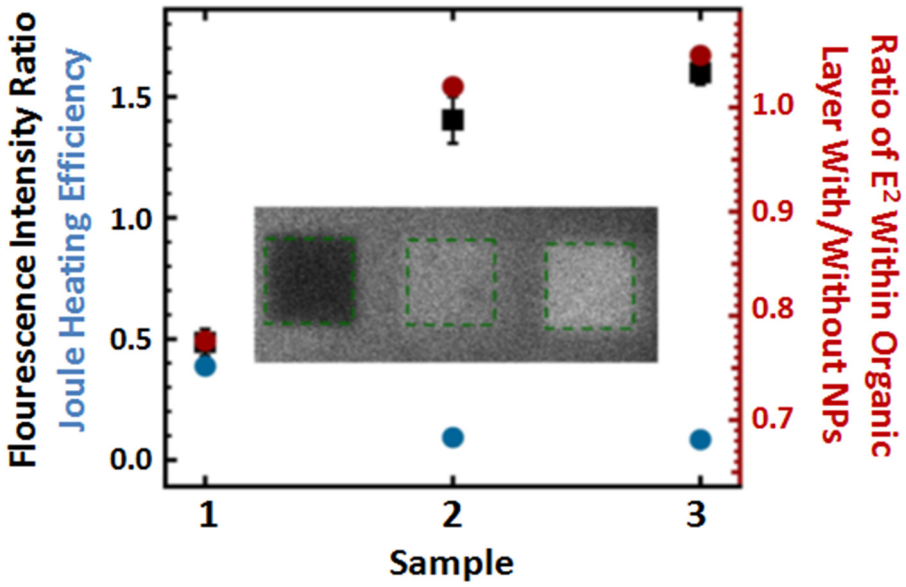

Figure 4. (insert) Fluorescence map across three different P3HT:PCBM film-covered NP arrays #1 to #3 indicated by the green dashed squares for W = 95 nm × P = 180 nm (**left** square), W = 95 nm × P = 300 nm (**center** square), and W = 180 nm × P = 360 nm (**right** square). The image was measured with a scanning laser microscope using a 633 nm wavelength source, collecting fluorescence at wavelengths above 660 nm. The black solid squares show the ratio of the fluorescent intensity from the corresponding areas with nanopillar arrays compared to that without NP-array. The red solid circles show the corresponding ratios of calculated $|E|^2$ integrated over the P3HT:PCBM volume not shadowed by nanopillars compared to that without NP-arrays. The blue solid circles are the corresponding calculated Joule heating efficiencies. Normal incident light from glass substrate side with 633 nm wavelength is used for the calculations.

The image was measured with a scanning laser microscope using a 633 nm wavelength source, collecting fluorescence at wavelengths above 660 nm [17]. The visible square regions in the map are from three Au nanopillar arrays; the pillar width and pitch are (left square) W = 95 nm × P = 180 nm, (center square) W = 95 nm × P = 300 nm, and (right square) W = 180 nm × P = 360 nm. The corresponding most intense extinction peaks for these arrays occur at 654 nm, 664 nm, and 830 nm, respectively.

It is clear that the field enhancement is absent in the NP array (left square) whose extinction peak most nearly coincides the excitation wavelength! Compared to the surrounding unpatterned area, the lower intensity in this pattern instead suggests a reduction of the field strength within the organic layer. For the arrays of the center and right squares in the map the most intense peak in the measured extinction is increasingly far from the wavelength of the 633 nm excitation wavelength, yet the

fluorescence intensity from the NP array increases. This trend is illustrated by black solid squares in the plot of Figure 4, which represent the ratio between the average fluorescent intensity on the NP-patterned area to that from the un-patterned area. For the arrays with W = 95 nm × P = 300 nm (center image) and with W = 180 nm × P = 360 nm (right image) we see a slight enhancement in the fluorescence. The solid red circles in Figure 4 show the ratio of the calculated $|E|^2$, integrated over the volume of P3HT:PCBM not occupied by Au nanopillars, to that calculated for the unpatterned substrate. The visual agreement between these two ratios as the width and pitch of the NP' are changed, and the lower value of the calculated $|E|^2$ over the W = 95 nm × P = 180 nm NP array confirms that attenuation, rather than enhancement in field strength occurs in the active layer at peak extinction.

It has recently been suggested by Atwater and Polman [22], that depending on their size, inclusion of noble metal particles in OSC's may result in ohmic loss which competes with scattering of the incident light. In addition, Mie Theory predicts that for smaller particles absorption within the particles dominates scattering. We thus consider the possibility that the extra extinction in the smaller width NP arrays we have studied is dominated by nanopillar absorption, and estimate how much of the power absorbed by the nanopillars in our arrays goes to Joule heating [23–25]. (Note that in the measured extinction spectra of Figure 2b, the back electrode is absent; while in the calculation for Joule heating efficiency presented here it is included.) Using the complex Poynting vector theorem, the time-average Ohmic loss within an Au nanopillar [26] can be expressed as:

$$P(\lambda) = \frac{1}{2}\iiint \sigma(\lambda)\left|E(x,y,z)\right|^2 dxdydz \tag{2}$$

where is the conductivity, is the local electrical field squared, and the integration is over the volume of a nanopillar. The relationship between the relative complex permittivity, and the complex refractive index, $n + ik$, is [27]:

$$\varepsilon_r = (1+\chi) + i\sigma / \omega\varepsilon_0 = (n^2 - k^2) + i2nk \tag{3}$$

where χ is the electrical susceptibility; and ε_0 is the permittivity. Thus, the conductivity can be expressed as:

$$\sigma(\lambda) = 2nk\omega\varepsilon_0 = 4\pi nkc\varepsilon_0 / \lambda \tag{4}$$

Combining these expressions, the Ohmic loss within the Au nanopillars is calculated, and the Joule heating efficiency, $A_{NP}(\lambda)$, is determined by dividing $P(\lambda)$ by the incident optical intensity. The green curves in Figure 5a–c show the Joule heating efficiency for OSC devices with nanopillar arrays with (a) W = 95 nm × P = 200 nm; (b) W = 135 nm × P = 270 nm; and (c) W = 180 nm × P = 360 nm. It reaches a maximum value at a wavelength nearly coincident with the extinction peak for the smaller, W = 95 nm × P = 200 nm array. The Joule heating is also considerably smaller for the larger nanopillars in this spectral range. As the width of the nanopillar increases, the Joule heating efficiency peak red-shifts with decreasing maximum heights. The blue curves in Figure 5 show for each device the total absorbance $A_{total}(\lambda)$, which is the sum of the calculated absorbance of the P3HT:PCBM film (red curves) and the calculated Joule heating efficiency (green curve). Compared to the extinction spectra shown in Figure 2b, we see similar broadening in total absorbance spectra, suggesting that Joule heating contributes to the observed broadening in the extinction spectra. Especially for the case

of the device with W = 95 nm × P = 200 nm pillars, the peak in the total absorbance $A_{total}(\lambda)$, appears near the measured peak in extinction, 657 nm, and is dominated by the Joule heating contribution.

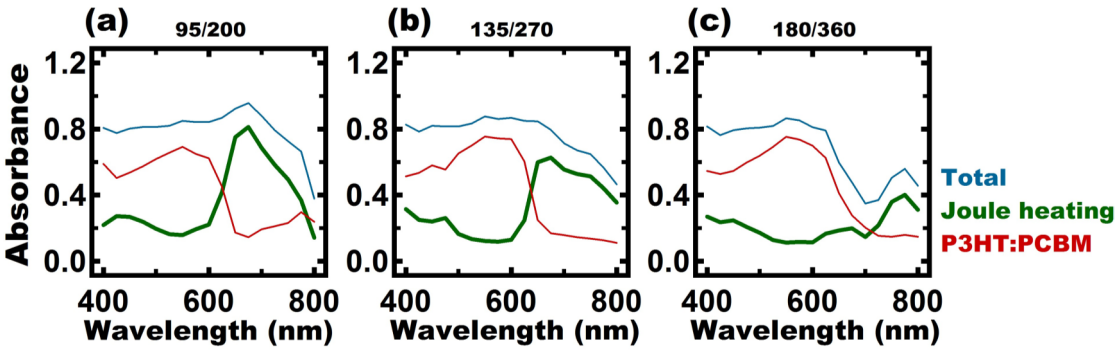

Figure 5. Calculated Joule heating efficiency (green curve), calculated P3HT:PCBM absorbance (red curve), and sum of both (blue curve) for NP-patterned devices. (**a**–**c**) for arrays with W = 95 nm × P = 200 nm, W = 135 nm × P = 270 nm, W = 180 nm × P = 360 nm, respectively. Nanopillar height is 70 nm for these arrays.

Figure 6a–c show the calculated spatial distribution of $|E|^2$ within a plane cutting though the center a nanopillar for an array with W = 95 nm × P = 200 nm, under normal incidence illumination at λ = 525 nm, 660 nm, and 750 nm, respectively. Near the peak in extinction (660 nm), the field within Au nanopillars is significantly more intense than that at 525 nm. Although local field enhancement is observed in close proximity to the nanopillar surface, the total field intensity integrated over the P3HT:PCBM layer is lower than that for the control device without nanopillars, consistent with the fluorescence image in Figure 4. This indicates there is a tradeoff between the transmission and the absorption/scattering. Interestingly, for the wavelength beyond the peak in extinction, *i.e.*, at 750 nm, the local field enhancement near the surface gives rise to a 65% increase in the calculated organic layer absorbance; this is in qualitative, but not quantitative agreement with the slight increase in measured EQE, ~14%. The discrepancy might be due to the fact that measured photocurrent is very low beyond 720 nm wavelength, making it difficult to distinguish the difference in EQE with and without nanopillars beyond this wavelength. Our field-squared maps in Figure 6b,c show that the enhancement is confined to a region within approximately 40 nm of the nanopillar surface. The very local nature of the intense field seemingly justifies our omitting a PEDOT:PSS interface layer (typically ~40 nm thick) in our devices.

The calculated Joule heating efficiency, shown by blue solid circles in the plot of Figure 4 displays a nearly opposite variation with NP width and pitch as that of the measured fluorescence intensity ratio; the fluorescence thus scales with $|E|^2$ within the P3HT:PCBM film, but not within the Au nanopillars.

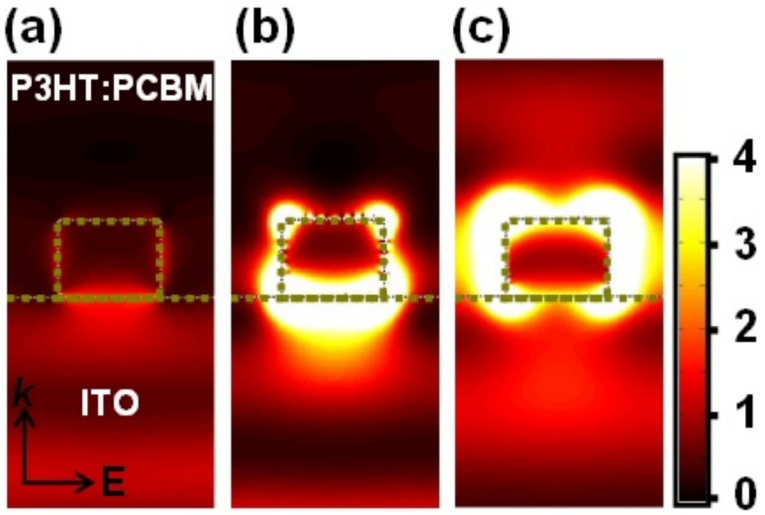

Figure 6. (**a**–**c**) Cross sectional $|E|^2$ maps, cutting though the center of the nanopillar for devices with NP-patterned arrays with W = 95 nm × P = 200 nm, and height = 70 nm. The incident optical wavelengths from left to right are 525 nm, 660 nm, and 750 nm.

3. Experimental Section

Our device architecture is illustrated schematically in Figure 1a above. A layer of indium tin oxide (ITO) of thickness 200 nm was used as high work function anode and a 300 nm thick aluminum (Al) layer was used as a low work function cathode. We defined square arrays of square cross-sectional Au nanopillars (NP) on the ITO- anode using electron-beam lithography; details of our fabrication method have been discussed elsewhere [18]. Scanning electron microscope (SEM) images of nanopillar arrays are shown in Figure 1b–e. Individual pillars in these images are: (b) approximately 95 nm in width, spaced at pitch of 150 nm; (c) 95 nm in width, spaced at pitch of 200 nm; (d) 95 nm in width, spaced at a pitch of 300 nm; and (e) 180 nm in width, spaced at a pitch of 360 nm; in each case the pillar heights are approximately 70 nm. The images show notable rounding of the corners of the pillars, presumably due to the proximity effect in electron beam lithography. The total pattern size in each case is 120 μm × 120 μm, however the region in which the active organic layer overlaps the anode and cathode is much larger, 2.5 mm × 2.5 mm. We thus created an opaque mask, consisting of a 200 nm thick Au film and 100 nm insulator of aluminum oxide, around the NP-patterned area to ensure that the measured photocurrent comes almost entirely from the region of the nanopillar pattern. The active device area of the BHJ cells is thus approximately 1.4×10^4 μm^2, of which a fraction given by the square of the ratio of the width to pitch is "shadowed" by the pillars themselves; this fraction ranges from 0.10 for the 95 nm × 300 nm patterns to 0.40 for the 95 nm × 300 nm pillar arrays studied here. The oxide layer was added to prevent a short circuit between the Al (top) and ITO (bottom) electrodes. We spun-cast a solution of regioregular P3HT and PCBM with weight ratio 1:1 in dichlorobenzene (DCB) onto each Au NP-patterned layer. Immediately after this, each film was "solvent dried", *i.e.*, placed in a covered glass container with a small amount of DCB added into the bottom, for 30 min. The typical thickness of the resulting active layer was determined to be approximately 220 nm. These latter two steps were carried out in an inert nitrogen gas atmosphere inside a glove box to minimize

photo-oxidative degradation. A nonstoichiometric titanium oxide (TiOx) precursor solution [28] was subsequently spun-cast onto the P3HT:PCBM composite, resulting in a 30 nm thick oxygen-getter layer. To maximize the volume of P3HT/PCBM in which a particle plasmon-enhanced field occurs, no poly(3,4-ethylenedioxythiophene):poly(styrenesulfonate) (PEDOT:PSS) layer was used between the pillars and the organic layer in our devices. A control cell was fabricated on each sample, using the same architecture, but omitting the nanopillar arrays. Finally, we carried out optical transmission measurements through our devices using a Cary 5000 UV-Vis-NIR spectrophotometer (Agilent Technologies, Santa Clara, CA, USA).

To model our results we first determined the complex refractive index, n + ik, of ITO and P3HT:PCBM by ellipsometry. Optical constants for glass [29], Au [30], titanium oxide [31], and Al [32] were taken from literature values. We calculated the optical field within our devices via the finite difference time-domain (FDTD) method [33,34] with grid size 3 nm for 95 nm size of pillars and 5 nm for larger pillars. Based upon the calculated local field $E_A(x,y,z)$, we next find the absorbed optical power per unit volume within the active layer, which is given by $Q_A(x,y,z) = 2\pi c\varepsilon_o n_A k_A |E_A(x,y,z)|^2 / \lambda$. Finally the absorbance A(λ) is calculated by dividing the integration of Q_A over the volume of the active layer by the incident optical intensity [14].

4. Conclusions

In summary, we find that our prototype Au nanopillar-patterned devices show a broadening in measured P3HT:PCBM extinction spectra in the form of an additional peak in the red part of the spectrum whose position depends on the size and spacing of the pillars. However, this NP-associated peak is absent in the measured external quantum efficiency spectrum, which instead shows a decrease at the corresponding wavelength. The calculated variation of the local electric field-squared, and absorption within the active layer with wavelength on the other hand follow that of the measured external quantum efficiency. We find that near the resonance wavelength, significant power is absorbed by the small nanopillars, due to the excitation of particle plasmons. Direct measurements show no obvious associated increase in fluorescence from the P3HT:PCBM active layer in the presence of Au nanopillars. Our results instead indicate that the energy associated with the extra peak in extinction is seemingly lost by Joule heating within the nanopillars, and suggest that enhancement of OSC efficiency by metallic nanostructures will require characteristic nanostructure dimensions considerably larger than those which have usually been explored.

Supplementary Materials

Supplementary materials can be accessed at: http://www.mdpi.com/1996-1073/8/3/1547/s1.

Acknowledgments

We thank Ben Palmer for allowing us access to the e-beam lithography system used in fabricating the nanopillar arrays, Dong Hun Park for providing us access and assistance in using an ellipsometry system, and Victor Yun for fabrication of shadow masks. We acknowledge useful conversations with Danilo Romero and Warren Herman. We are grateful to acknowledge the use of TEMPEST FDTD

software, provided by Professor A. Neureuther of the University of California at Berkeley. This work was supported by the Laboratory for Physical Sciences.

Author Contributions

S.-J.T. performed the designs, fabrications, measurements, analysis and simulations, and largely wrote this article. M.B. contributed technical expertise in the OPV experimental design and EQE measurement. H.-C.K. contributed to the analysis. R.J.P. contributed to the experimental design, project management, analysis, and the writing of this article.

Conflicts of Interest

The authors declare no conflict of interest.

References

1. Li, G.; Shrotriya, V.; Huang, J.S.; Yao, Y.; Moriarty, T.; Emery, K.; Yang, Y. High-efficiency solution processable polymer photovoltaic cells by self-organization of polymer blends. *Nat. Mater.* **2005**, *4*, 864–868.
2. Chen, H.Y.; Hou, J.H.; Zhang, S.Q.; Liang, Y.Y.; Yang, G.W.; Yang, Y.; Yu, L.P.; Wu, Y.; Li, G. Polymer solar cells with enhanced open-circuit voltage and efficiency. *Nat. Photonics* **2009**, *3*, 649–653.
3. NREL National Center for Photovoltaics Research Cell Efficiency Records. Available online: http://www.nrel.gov/ncpv/images/efficiency_chart.jpg (accessed on 11 December 2014).
4. Cole, J.R.; Halas, N.J. Optimized plasmonic nanoparticle distributions for solar spectrum harvesting. *Appl. Phys. Lett.* **2006**, *89*, 153120.
5. Morfa, A.J.; Rowlen, K.L.; Reilly, T.H.; Romero, M.J.; van de Lagemaat, J. Plasmon-enhanced solar energy conversion in organic bulk heterojunction photovoltaics. *Appl. Phys. Lett.* **2008**, *92*, 013504.
6. Lee, J.H.; Park, J.H.; Kim, J.S.; Lee, D.Y.; Cho, K. High efficiency polymer solar cells with wet deposited plasmonic gold nanodots. *Org. Electron.* **2009**, *10*, 416–420.
7. Kim, S.S.; Na, S.I.; Jo, J.; Kim, D.Y.; Nah, Y.C. Plasmon enhanced performance of organic solar cells using electrodeposited Ag nanoparticles. *Appl. Phys. Lett.* **2008**, *93*, 073307.
8. Chen, X.H.; Zhao, C.C.; Rothberg, L.; Ng, M.K. Plasmon enhancement of bulk heterojunction organic photovoltaic devices by electrode modification. *Appl. Phys. Lett.* **2008**, *93*, 123302.
9. Yoon, W.J.; Jung, K.Y.; Liu, J.W.; Duraisamy, T.; Revur, R.; Teixeira, F.L.; Sengupta, S.; Berger, P.R. Plasmon-enhanced optical absorption and photocurrent in organic bulk heterojunction photovoltaic devices using self-assembled layer of silver nanoparticles. *Sol. Energy Mater. Sol. Cells* **2010**, *94*, 128–132.
10. Qiao, L.F.; Wang, D.; Zuo, L.J.; Ye, Y.Q.; Qian, J.; Chen, H.Z.; He, S.L. Localized surface plasmon resonance enhanced organic solar cell with gold nanospheres. *Appl. Energy* **2011**, *88*, 848–852.

11. Ferry, V.E.; Verschuuren, M.A.; Li, H.; Schropp, R.E.I.; Atwater, H.A.; Polman, A. Improved red-response in thin film a-Si:H solar cells with soft-imprinted plasmonic back reflectors. *Appl. Phys. Lett.* **2009**, *95*, 183503.
12. Topp, K.; Borchert, H.; Johnen, F.; Tune, A.V.; Knipper, M.; von Hauff, E.; Parisi, J.; Al-Shamery, K. Impact of the incorporation of au nanoparticles into polymer/fullerene solar cells. *J. Phys. Chem. A* **2010**, *114*, 3981–3989.
13. Tsai, S.; Ballarotto, M.; Romero, D.B.; Herman, W.N.; Kan, H.; Phaneuf, R.J. Effect of gold nanopillar arrays on the absorption spectrum of a bulk heterojunction organic solar cell. *Opt. Express* **2010**, *18*, A528–A535.
14. Kelly, K.L.; Coronado, E.; Zhao, L.L.; Schatz, G.C. The optical properties of metal nanoparticles: The influence of size, shape, and dielectric environment. *J. Phys. Chem. B* **2003** *107*, 668–677.
15. Jin, R.C.; Cao, Y.W.; Mirkin, C.A.; Kelly, K.L.; Schatz, G.C.; Zheng, J.G. Photoinduced conversion of silver nanospheres to nanoprisms. *Science* **2001**, *294*, 1901–1903.
16. Haynes, C.L.; McFarland, A.D.; Zhao, L.L.; van Duyne, R.P.; Schatz, G.C.; Gunnarsson, L.; Prikulis, J.; Kasemo, B.; Kall, M. Nanoparticle optics: The importance of radiative dipole coupling in two-dimensional nanoparticle arrays. *J. Phys. Chem. B* **2003**, *107*, 7337–7342.
17. Guo, S.H.; Tsai, S.J.; Kan, H.C.; Tsai, D.H.; Zachariah, M.R.; Phaneuf, R.J. The effect of an active substrate on nanoparticle-enhanced fluorescence. *Adv. Mater.* **2008**, *20*, 1424–1429.
18. Corrigan, T.D.; Guo, S.H.; Szmacinski, H.; Phaneuf, R.J. Systematic study of the size and spacing dependence of Ag nanoparticle enhanced fluorescence using electron-beam lithography. *Appl. Phys. Lett.* **2006**, *88*, 101112.
19. Ditlbacher, H.; Krenn, J.R.; Felidj, N.; Lamprecht, B.; Schider, G.; Salerno, M.; Leitner, A.; Aussenegg, F.R. Fluorescence imaging of surface plasmon fields. *Appl. Phys. Lett.* **2002**, *80*, 404–406.
20. Guo, S.H.; Heetderks, J.J.; Kan, H.C.; Phaneuf, R.J. Enhanced fluorescence and near-field intensity for Ag nanowire/nanocolumn arrays: Evidence for the role of surface plasmon standing wave. *Opt. Express* **2008**, *16*, 18417–18425.
21. Guo, S.H.; Britti, D.G.; Heetderks, J.J.; Kan, H.C.; Phaneuf, R.J. Spacer layer effect in fluorescence enhancement from silver nanowires over a silver film; switching of optimum polarization. *Nano Lett.* **2009**, *9*, 2666–2670.
22. Atwater, H.A.; Polman, A. Plasmonics for improved photovoltaic devices. *Nat. Mater.* **2010**, *9*, 205–213.
23. Cole, J.R.; Mirin, N.A.; Knight, M.W.; Goodrich, G.P.; Halas, N.J. Photothermal efficiencies of nanoshells and nanorods for clinical therapeutic applications. *J. Phys. Chem. C* **2009**, *113*, 12090–12094.
24. Govorov, A.O.; Zhang, W.; Skeini, T.; Richardson, H.; Lee, J.; Kotov, N.A. Gold nanoparticle ensembles as heaters and actuators: Melting and collective plasmon resonances. *Nanoscale Res. Lett.* **2006**, *1*, 84–90.
25. Govorov, A.O.; Richardson, H.H. Generating heat with metal nanoparticles. *Nano Today* **2007**, *2*, 30–38.
26. Cheng, D.K. *Field and Wave Electromagnetics*; Addison-Wesley: New York, NY, USA, 1982; p. 326.

27. Craig, D.R.H.; Bohren, F. *Absorption and Scattering of Light by Small Particles*; Wiley-VCH: Weinheim, Germany, 2004; pp. 227–231.
28. Lee, K.; Kim, J.Y.; Park, S.H.; Kim, S.H.; Cho, S.; Heeger, A.J. Air-stable polymer electronic devices. *Adv. Mater.* **2007**, *19*, 2445–2449.
29. Zudans, I.; Heineman, W.R.; Seliskar, C.J. *In situ* measurements of chemical sensor film dynamics by spectroscopic ellipsometry. Three case studies. *Thin Solid Films* **2004**, *455*, 710–715.
30. Johnson, P.B.; Christy, R.W. Optical-constants of noble-metals. *Phys. Rev. B* **1972**, *6*, 4370–4379.
31. Rantala, J.T.; Karkkainen, A.H.O. Optical properties of spin-on deposited low temperature titanium oxide thin films. *Opt. Express* **2003**, *11*, 1406–1410.
32. Smith, D.Y.; Shiles, E.; Inokuti, M. Handbook of optical constants of solids. In *Handbook of Optical Constants of Solids, Vol. 1*; Palik, E.D., Ed.; Academic Press Handbook: New York, NY, USA, 1985; pp. 369–406.
33. Pistor, T. *Generalizing the TEMPEST FDTD Electromagnetic Simulation Program*; Electronics Research Laboratory, College of Engineering, University of California: Berkeley, CA, USA, 1997.
34. Yee, K.S. Numerical solution of initial boundary value problems involving maxwell's equation in isotropic media. *IEEE Trans. Antennas Propag.* **1966**, *14*, 302–307.